Ore Geology Reviews 140 (2022) 104599

Contents lists available at ScienceDirect

Ore Geology Reviews

journal homepage: www.elsevier.com/locate/oregeorev

# Formation of the Chah-Gaz iron oxide-apatite ore (IOA) deposit, Bafq District, Iran: Constraints from halogens, trace element concentrations, and Sr-Nd isotopes of fluorapatite

Fatemeh Sepidbar [a,*], Ghasem Ghorbani [a,*], Adam C. Simon [b], Jinlong Ma [c], Richard M Palin [d], Seyed Masoud Homam [e]

[a] School of Earth Sciences, Damghan University, Damghan 36716-41167, Iran
[b] Department of Earth and Environmental Sciences, University of Michigan, 1100 North University Avenue, Ann Arbor, MI 48109-1005, USA
[c] State Key Laboratory of Isotope Geochemistry, Guangzhou Institute of Geochemistry, Chinese Academy of Sciences, Guangzhou 510640, PR China
[d] Department of Earth Sciences, University of Oxford, Oxford, UK
[e] Department of Geology, Faculty of Science, Ferdowsi University of Mashhad, Mashhad, Iran

ARTICLE INFO

*Keywords:*
Halogens
Trace elements
Sr-Nd isotopes
Magmatic-hydrothermal system
Chah-Gaz

ABSTRACT

The textures, chemistry and Sr-Nd isotopic compositions of apatite from the Chah-Gaz iron-oxide apatite (IOA) deposit in the Bafq metallogenic belt, central Iran, were studied to investigate the formation of this ore deposit. Two generations of apatite were recognized based on Cl/F and Cl/OH ratios. Primary fluorapatite, which is coeval with magnetite in the massive ore bodies, is chemically homogeneous and characterized by Cl/F < 0.05 and Cl/OH in the range of 0.01–0.07. By contrast, F-depleted apatite rims are present in apatite hosted in veinlets that crosscut the massive ore bodies and are disseminated in the igneous host rocks, and have Cl/F and Cl/OH-apatite ratios of 0.08–0.12 and 0.15–0.79, respectively. The F-depleted rims are also depleted in LREEs, Th and U, consistent with the presence of secondary monazite, xenotime and thorite that formed by coupled dissolution-reprecipitation. The whole-rock Nd–Sr isotopic data ($(^{87}Sr/^{86}Sr)_{(i)}$ = 0.7052 to 0.7064 and εNd(t) = +1.3 to + 2.7) of gabbro-diorite indicate an mantle source, while the high -K, calc-alkaline-shoshonitic volcanic host rocks have εNd(t) = − 5.5 to − 7.6, clearly reflecting mixing between mantle-derived mafic magmas and assimilated Proterozoic basement. The initial $^{87}Sr/^{86}Sr$ ratios and εNd values of both F-rich and -depleted apatites (0.7038 to 0.7050 and −0.3 to + 6.5, respectively) are similar to gabbroic rocks and support a magmatic source for primary fluorapatite, with minimal or no crustal contribution, and indicate that the magmatic event with negative εNd values did not affect the whole-rock Sm-Nd signature of the ore. Petrography plus geochemical and Nd-Sr isotopic data of both studied fluorapatite, which come from iron oxide stage, are consistent with a combined igneous/magmatic-hydrothermal genesis for the Chah-Gaz IOA deposit, with low degrees of hydrothermal overprint, as evidenced by the formation of F-depleted (Cl-rich) apatite rims. The relatively constant Sr-Nd data in apatite are consistent with superimposed, episodic hydrothermal fluids from the same, evolving, magmatic-hydrothermal system.

## 1. Introduction

Halogen and trace element concentrations as well as Sr-Nd isotopes in apatite, $Ca_{10}(PO_4)_6$(F, Cl, OH), have proven to be particularly helpful in unravelling mineralization processes that form magnetite-rich iron oxide-apatite (IOA) deposits (Harlov et al., 2002; Daliran et al., 2010; Jonsson et al., 2016; Bonyadi et al., 2011; La Cruz et al., 2019, 2020; Palma et al., 2019). The halogens (F and Cl) and trace and rare earth elements in apatite are extremely sensitive to changes in the composition of silicate melts and hydrothermal fluids (Palma et al., 2019; Heidarian et al., 2018). Not surprisingly, apatite chemistry is often used in the study of the volatile behaviour in igneous and magmatic-hydrothermal systems (La Cruz et al., 2019, 2020; Palma et al., 2019) and development of potentially REE-enriched-apatite mineral systems, including Kiruna-type IOA deposits (Prowatke and Klemme, 2006; La Cruz et al., 2019, 2020; Palma et al., 2019).

* Corresponding authors.
*E-mail addresses:* f.sepidbar@ut.ac.ir (F. Sepidbar), ghorbani@du.ac.ir (G. Ghorbani).

https://doi.org/10.1016/j.oregeorev.2021.104599
Received 14 June 2021; Received in revised form 16 November 2021; Accepted 21 November 2021
Available online 7 December 2021

The genesis of IOA deposits remains a topic of debate. Some studies propose a purely magmatic process wherein a parent silicate melt unmixed into conjugate Si-rich melt and Fe-P-rich melt with complete mechanical separation of the two melts and crystallization of the Fe-P-rich melt to form an IOA deposit (e.g., Nystrom and Henriquez, 1994; Velasco et al., 2016; Hou et al., 2018). Other studies have proposed a purely hydrothermal model, in which Fe-rich magmatic or basinal fluids reacted with volcanic host rocks to form replacement IOA ore bodies (e.g., Sillitoe and Burrows, 2002; Barton and Johnson, 2004; Dare et al., 2015). A third proposed genetic model invokes a combination of magmatic and magmatic-hydrothermal processes, where in igneous magnetite and apatite serve as nucleation sites for the exsolution of magmatic-hydrothermal fluid that results in the formation of a magnetite-apatite-fluid suspension that evolves from the source magma and forms IOA mineralization in the superjacent environment (Knipping et al., 2015a, b; Ovalle et al., 2018; Simon et al., 2018; Knipping et al., 2019; La Cruz 2019; 2020). This latter model is commonly referred to as the flotation model wherein igneous magnetite and apatite nano- and micro-lites grow larger by sourcing their essential structural constituents from the Fe-, Ca-, P-, Cl-bearing magmatic-hydrothermal ore fluid during decompression and cooling.

The role of the halogens F and Cl in the formation of IOA deposits remains poorly understood. Apatite in IOA deposits is a mineral phase of particular interest in this regard because it is the predominant F and Cl-bearing phase and its structure has a tendency to incorporate and concentrate trace elements such as Sr, U, Th, REE, Y, S, and As (Prowatke and Klemme, 2006; Konecke et al., 2017; Kim et al., 2017). Field (e.g., Hansen and Harlov, 2007) and e xperimental studies (e.g., Harlov and Forster, 2003; Harlov et al., 2005; Betkowski et al., 2016) demonstrate that the F, Cl and OH concentrations in apatite and the existence of secondary monazite, xenotime and/or thorite inclusions in apatite provide insights for the processes that form IOA deposits (e.g., Harlov et al., 2002; Jonsson et al., 2016; La Cruz et al., 2019). The Sr and Nd isotope compositions of apatite from IOA deposits and their related igneous host rocks can be also used as a petrogenetic indicator to distinguish between mantle-derived magmatic versus crustal, hydrothermal sources (e.g., Zhao et al., 2015; Zeng et al., 2016; Palma et al., 2019).

In this study, we used a combination of petrography, mineral chemistry and Sr-Nd isotopic data from apatite grains, and whole rock geochemistry and isotopic data for the igneous host rocks from the Chah-Gaz IOA deposit in the Bafq iron metallogenic belt in central Iran, to elucidate the genesis of IOA deposits in one of the world's foremost IOA districts, containing>2 billion tons of iron ore. Several studies proposed a purely magmatic genesis for the Baqf IOA deposits (Mokhtari et al., 2013), whereas Daliran et al. (2010), and Torab and Lehmann (2007) proposed that high-temperature hydrothermal fluids were responsible for the formation of the Bafq IOA deposits. Taghipour et al. (2013) proposed that a combination of magmatic and hydrothermal fluids produced iron oxide mineralization in the Choghart deposit. Ziapour et al. (2021) proposed that an iron-rich magmatic-hydrothermal fluid generated the massive magnetite-rich ore bodies in the Chah-Gaz IOA deposit. Each of the aforementioned studies increased our understanding of the origin of the Baqf IOA deposits by focusing on the composition of magnetite, whereas comprehensive investigations of apatite, a ubiquitous phase in the Baqf IOA deposits and similar deposits globally, remains understudied. The textural and compositional data for apatite from the Chah-Gaz IOA deposit are consistent with formation of the deposit by a combination of igneous and magmatic-hydrothermal processes as described in the flotation model proposed by Knipping et al. (2015a).

## 2. Geology of the Bafq iron metallogenic belt

The Bafq iron metallogenic belt is located in the Early Cambrian Kashmar-Kerman volcano-plutonic arc in Central Iran that formed during subduction of the Proto-Tethys oceanic plate (Ramezani and Tucker, 2003; Torab and Lehmann, 2007). Most of the IOA deposits in the Bafq district are located in the center of the Kashmar-Kerman tectonic zone (Ramezani and Tucker, 2003) (Fig. 1a), which is an arcuate N-S-trending zone approximately 600 km long and 25 km wide. This belt includes a thick sequence of Precambrian basement rocks, covered by Paleozoic and younger sedimentary rocks. The Precambrian basement in the Bafq iron metallogenic belt is comprised of gneiss, anatectic granite, migmatite and amphibolite of the Chapedony Complex, which is overlain by the Boneh-Shurow Complex, the Tashk/Morad Formation and the Cambrian volcano-sedimentary unit (CVSU) of the Rizu and Dezu formations (Ramezani and Tucker, 2003) (Fig. 1B). The Boneh-Shurow Complex (Haghipour and Pelissier, 1977) is a metamorphic series of gneiss, mica-schist and amphibolite, with subordinate dolomitic marble and mafic to intermediate magmatic intrusive bodies. A zircon U–Pb age of 544 ± 7 Ma has been interpreted as crystallization age of the granitic protolith(s) of the Boneh-Shurow gneiss (Ramezani and Tucker, 2003).

The Tashk/Morad Formation consists of graywacke interbedded with arkosic arenite, argillite, tuffaceous rocks and basaltic sills. The contact between the Tashk Formation and the Boneh-Shurow Complex is thrust-faulted (Fig. 1B). The Cambrian Rizu and Dezu formations were deposited in a Late Precambrian rifted basin (Ghorbani, 2013) and consist of carbonate, sandstone, shale and volcanic rocks. This rift succession overlies the sedimentary rocks of the Tashk Formation and is, in turn, overlain by an Upper Cambrian sequence of intercalated upper amphibolite-facies mica-schists and marble of the Sarkuh Complex (Hushmandzadeh, 1969). The Cambrian volcano-sedimentary unit of the Rizu and Dezu formations constitutes the principal host rocks of the IOA mineralization in the Bafq iron metallogenic belt. In addition, alkaline, felsic and mafic igneous rocks of Cadomian age with within plate-like geochemical characteristics which take place in the southeast (Sepidbar et al., 2020), northwest and as in exotic blocks in salt domes in south of Iran (Asadi et al., 2020), are also occurred as the Zarigan-Narigan units in central Iran.

Ramezani and Tucker (2003) reported ages of 528.2 ± 0.8 Ma and 527 ± 1 Ma for the Cambrian rhyodacite and dacite porphyry in the CVSU, which agree with U–Th–Pb ages of 515 ± 21 Ma and 529 ± 21 Ma determined on monazite inclusions within apatite crystals from the Choghart ore deposit (Torab and Lehmann, 2007). Statistically identical U-Pb zircon ages of 529 ± 16 Ma and 525 ± 7 Ma have been obtained on the Zarigan granite (Ramezani and Tucker, 2003). Stosch et al. (2011) reported $^{206}Pb/^{238}U$ ages of 539 ± 6 Ma and 527 ± 8 Ma for monazite from the Lakkeh Siah, and Zarigan. The Se-Chahun magnetite-apatite orebody formed at 510 ± 8 Ma (apatite U–Pb LA-ICP-MS age), at the end of the main regional sodic magmatic event dated at 525 ± 7 Ma (Bonyadi et al., 2011). The aforementioned published geochronological data and the close spatial relationship of IOA deposits and apatite-rich rocks with Lower Cambrian felsic volcanic rocks support the hypothesis that IOA mineralization in the Bafq district is genetically linked to broadly coeval Lower Cambrian magmatism (Daliran et al., 2010).

The larger deposits in the Bafq iron metallogenic belt are Chadormalu (400 Mt), Se-Chahun (140 Mt), Chah-Gaz (83.1 Mt), Esfordi (17 Mt), Mishdovan and Choghart (216 Mt) (Torab and Lehmann, 2007). Most deposits are characterized by massive to variably brecciated IOA ores (Bonyadi et al., 2011). The IOA mineralization was either simultaneous with, or slightly younger than the Zarigan and Narigan granite (s) and the volcanic rocks of the CVSU. As this study is focused on apatite, we chose the Chah-Gaz deposit, located in the northern part of the Bafq iron metallogenic belt (Fig. 1B), because it is particularly rich in apatite (~5–10 vol%).

### 2.1. The Chah-Gaz volcanic host rocks and associated IOA orebody

The Chah-Gaz magmatic complex occupies an area of ~ 5 $km^2$. It consists of rhyolite/rhyodacite of the CVSU, and granite and alkaline gabbro-diorite that occur as elongated bodies bounded by NW–SE faults (Fig. 2).

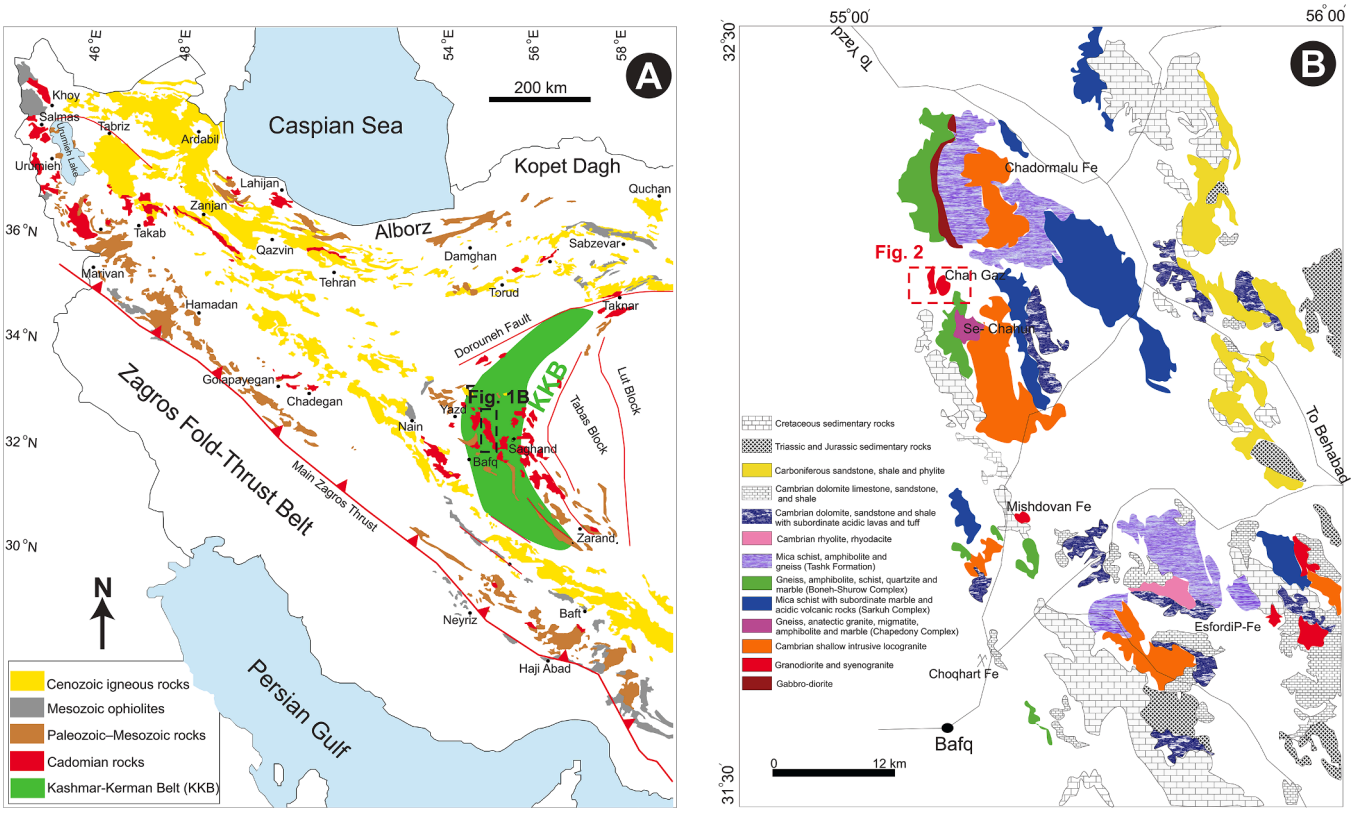


**Fig. 1.** (A) Geological map showing Cadomian basement rocks of Iran and location of IOA deposits in the Bafq district which are located in the center of the Kashmar-Kerman tectonic zone; (B) Basic geological map of the Bafq district in the Posht-e-Badam Block (modified after Ramezani and Tucker, 2003; Rajabi et al., 2015).

Aphyric to porphyritic dacitic and rhyodacitic rocks are the main ore host rocks in the Chah-Gaz area (Fig. 3A) and show a faulted contact with Infracambrian deformed sediments and a normal contact with granitoid. The host rocks contain resorbed quartz (~47 vol%), sanidine and plagioclase phenocrysts. The groundmass is microcrystalline to cryptocrystalline and consists of quartz and plagioclase–K-feldspar intergrowths. Accessory minerals include apatite, biotite and magnetite, while common secondary minerals include calcite, sericite, titanite, hematite and chlorite. Plagioclase phenocrysts are altered to epidote and calcite, and K-feldspar is often altered to sericite. Gabbro-diorite/diorite bodies in the Chah-Gaz area have granular to porphyritic textures, are generally medium-grained, and contain plagioclase (60 vol%), brown amphibole (20–30 vol%), clinopyroxene (5–10 vol%) and quartz (5–8 vol%) as the main primary constituents, although orthopyroxene and biotite occur in some samples. Opaque minerals and apatite are present as accessory minerals, whereas, epidote and chlorite are secondary minerals. Clinopyroxene is often altered to amphibole, and plagioclase is often altered to albite.

Magnetite-apatite mineralization originally formed a single ore body that was subsequently dissected into two ore bodies by a NW-SE strike-slip fault. Magnetite-apatite mineralization affected mainly altered rhyolite/rhyodacite and shallow felsic-intermediate subvolcanic rocks (Fig. 2). The host rocks experienced extensive *syn*-mineralization hydrothermal alteration, especially along NW-SE faults, which is characteristic of all mineral deposits in the Bafq district (Ziapour et al., 2021).

The shapes of the Chah-Gaz ore bodies follow the general orientation of the main NW-SE trending fault system, which correlates with lineaments formed during the arc-backarc development. In addition, intersections of fault sets, where transtensional transposition generated dilatational zones, appear as favourable sites of mineralization.

Two styles of mineralization are recognized at Chah-Gaz: massive magnetite-dominated ore that modally dominates (Fig. 3B) the deposit, and magnetite-apatite veins and veinlets that are related to iron oxide-stage, regional alteration and metasomatism of the host rock.

The massive ores are formed largely of magnetite with minor subhedral to anhedral apatite grains (Fig. 3C), along with minor hematite, and rare rutile, titanite, allanite, siderite and ankerite that have sharp interfaces with intercalated volcanic rocks. The outer areas of the massive ore bodies are mainly brecciated and display cataclastic texture. The magnetite-apatite veinlets include calcite ± magnetite ± apatite ± actinolite ± albite ± pyrite ± rutile ± titanite ± thorite ± allanite all of which are present within the altered host rocks (Fig. 3D) and the massive magnetite ore. In addition, minor monazite and xenotime can be also present in these veinlets. The apatite rims display an acicular texture (Fig. 3E).

The alteration was sodic-calcic, potassic, magnesian, silicic, sericitic, argillic and calcareous, depending on host rock lithology (Fig. 4). The sodic-calcic alteration zone is characterized by actinolite, albite, augite and epidote whereas potassic alteration is marked by K-feldspar as a late-stage phase that partially replaced albite of the older sodic-calcic alteration, and minor biotite and phlogopite, as well as sericitization. Magnesian alteration is limited to faults and is characterized mainly by serpentine, chlorite and talc. Silicic alteration is also younger than the sodic-calcic alteration, whereas sericitic and argillic alteration formed both during and after the sodic-calcic alteration. Carbonatization is the final hydrothermal alteration event in the deposit.

## 3. Analytical methods

### 3.1. Electron Probe MicroAnalyses (EPMA)

The concentrations of major element oxides in apatite grains in veinlet that cross-cut the Chah-Gaz altered host rocks and massive ore were determined at the Wuhan Technology University of China (WTU), Wuhan, using a JXA-8230 electron probe microanalyzer (EPMA). All analyses were performed using an accelerating voltage of 15 kV, a beam

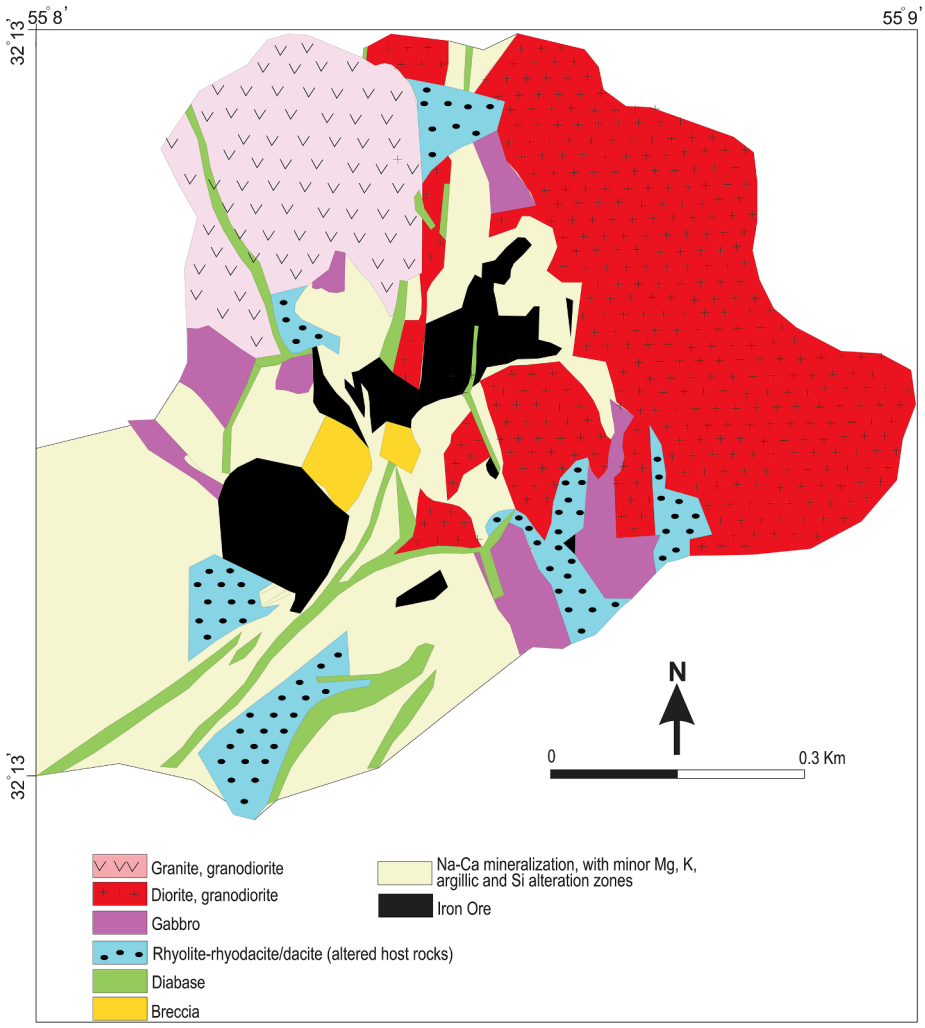


**Fig. 2.** Geological map of the Chah-Gaz showing mineralization zone and associated volcanic host rocks.

current of 20nA and a beam diameter of 20 μm. The standards employed here include natural apatite for analyses of F, Cl, Ca and P, and hornblende for Si and Fe. The Lα line was used for the measurements of Sr and Ba, and the Kα line for all other elements. The lower limit of detection is typically better than 0.05 wt%. For each mineral spot, the relatively mobile elements F and Na were analyzed first in order to prevent their potential loss over the course of the analysis. The analytical data acquired are provided in Supplementary Table 1. A correction for excess F due to third-order interference of P Kα on F Kα was applied. Excess F was estimated at about 0.35% based on 15 measurements of F Kα in a phosphate that does not contain F (reference monazite at Univ. Würzburg). The measurements yielded a mean of 0.040% "fake" F per % P. A similar value (0.045%) was obtained by Potts and Tindle (1989). Note that grain orientation and anisotropic ion diffusion can also have a substantial influence on the quantification of F with the electron microprobe (e.g., Stormer et al., 1993).

### 3.2. LA-ICP-MS

The concentrations of trace elements, including rare earth elements (REE), Mn, Sr and were determined on individualapatite grains by excimer LA-ICP-MS at the State Key Laboratory of Geological Processes and Mineral Resources, School of Earth Sciences, China University of Geoscience, Wuhan, China. The analytical data acquired are provided in Supplementary Table 1. The details of these analytical procedures and instrumental operating conditions are described in Gao et al. (2002). A spot size of 30–40 μm was used. The calcium content of the apatite obtained by EPMA was used as an internal standard, while NIST SRM 610 was used as an external standard to correct and monitor ion yield, matrix effects, and instrumental drift in the ICP-MS. The analysis procedure for each spot consisted of approximately 20 s of background and 50 s of data acquisition. The GLITTER 4.0 software was then used for data reduction. The accuracy and precision of the LA-ICP-MS settings were reported for the known international standards, including NIST SRM 610 (Gao et al., 2002). The precision of the analyses on the NIST SRM 610 in this study was better than below 2.5% for the trace elements. The limit of detection (LOD) of this method for most trace elements was well below the ppm level for all the analyzed elements.

### 3.3. ICP-MS

The concentrations of major elements in samples of dacite-rhyodacite host rocks were analysed at the Second Institute of Oceanography, Ministry of Natural Resources in China. Samples were ground to<200 mesh and fluxed with $Li_2B_4O_7$ (49.75 wt%), $LiBO_2$ (49.75 wt%) and LiBr (0.5 wt%) (with a sample/flux ratio of 1:10) to make homogeneous glass disks at 1100 °C using a FRONTII muffle furnace (The Instrument Company of China). Major element compositions were determined by X-ray fluorescence (XRF) in fused glass disks using a PANalytical Axiox spectrometer. Trace element analyses of whole rocks were conducted on an Elan DRC-e inductively coupled plasma mass spectrometer (ICP-MS) at the Key Laboratory of Submarine Geosciences,

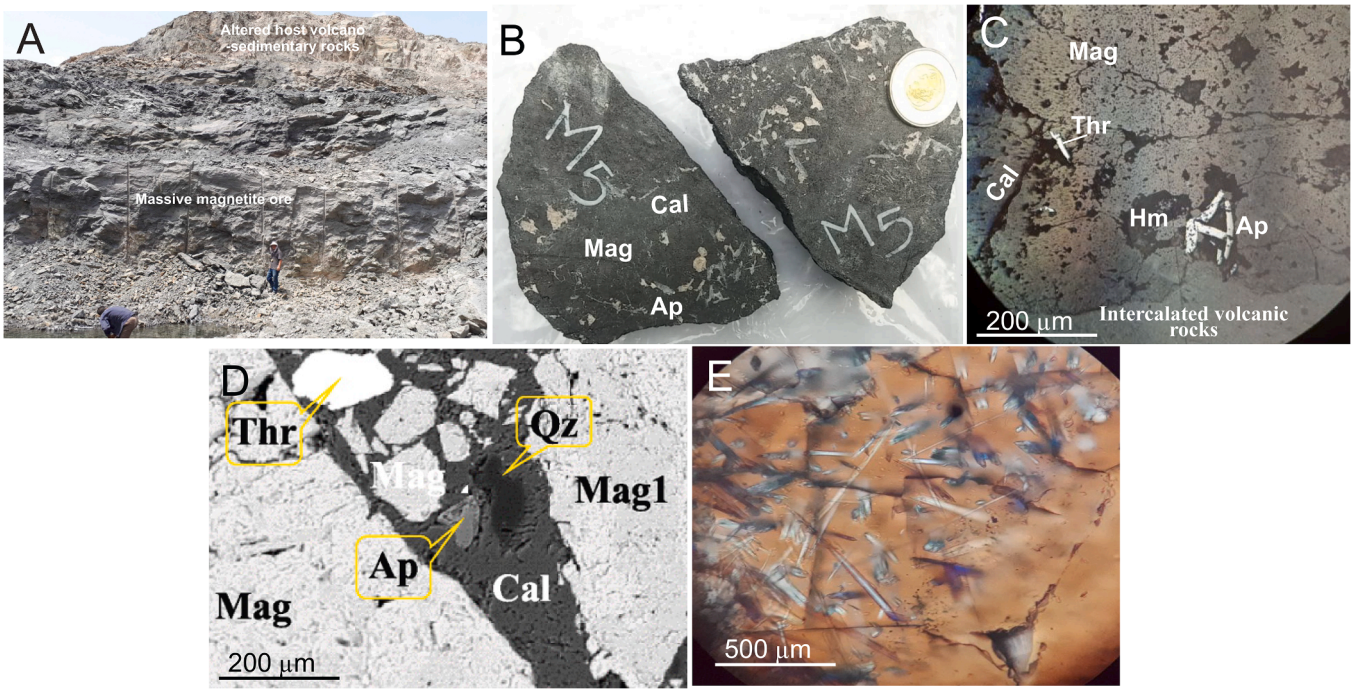


**Fig. 3.** (A) The contacts between altered host volcano-sedimentary rocks and Massive magnetite ore; (B) Apatite related to massive magnetite ore; (C) Minor subhedral to anhedral apatite grains within the massive magnetite ore; (D) Apatite related to magnetite-apatite within the veinlets include calcite ± magnetite ± apatite ± thorite which are present within the altered host rocks; (E) (F) Apatite with acicular texture within the veinlets of altered host rocks.

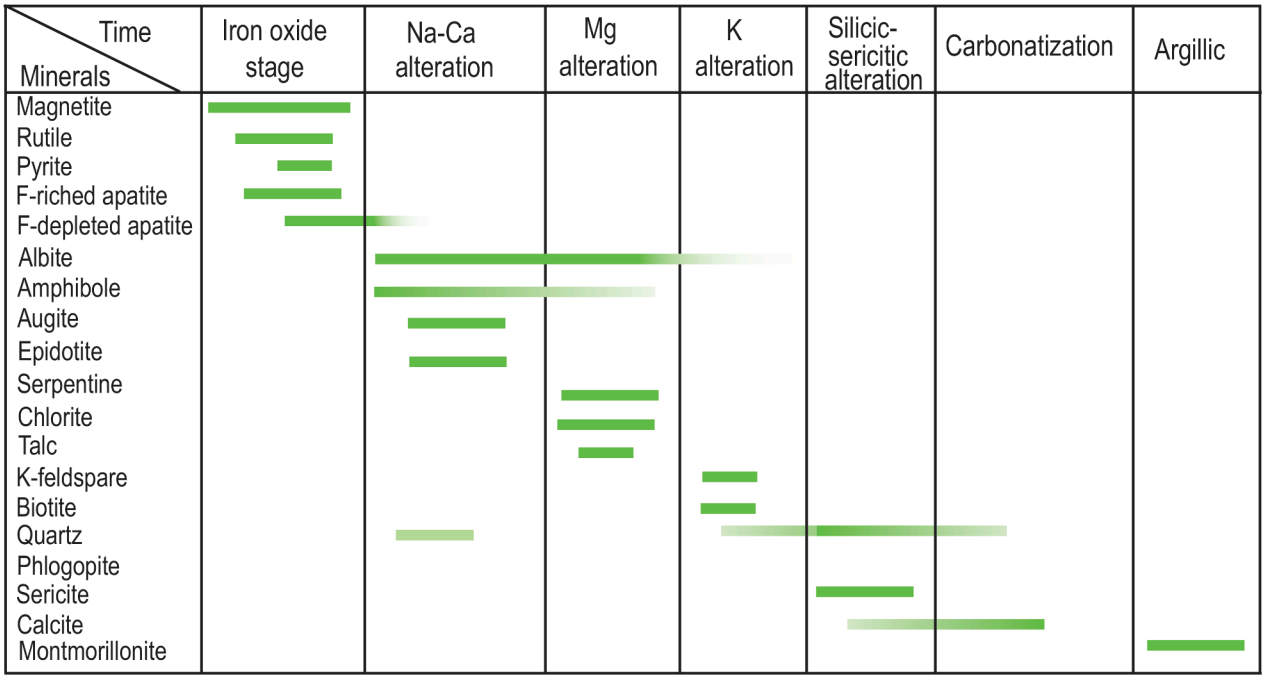


**Fig. 4.** Paragenetic sequence of ore minerals and the associated alteration assemblage in the Chahgaz mineral deposit (Heavy line: major phase; light line: minor phase).

Ministry of Natural Resources (MNR). The analytical data acquired are provided in Supplementary Table 2. Samples were powdered (200 mesh) and placed in an oven at 105 °C to dry for 12 h. Then, 50 mg of sample powder, 1.5 ml $HNO_3$, 1.5 ml HF, and 0.1 ml $HClO_4$ were accurately weighed, put into a Teflon bomb, and this was placed in a stainless steel pressure jacket and heated to 190 °C in an oven for 48 h. After cooling, the Teflon bomb was opened and placed on a hotplate at 140 °C and evaporated to incipient dryness. Then, 3 ml of 50% $HNO_3$ was added, and the Teflon bomb was resealed and placed in an oven at 190 °C for 12 h. After cooling, the final solution was transferred to a 100 ml polyethylene bottle, 1 ml (Rh + Re) mixed standard solution (1 mg/L) was added, and then diluted to 100 g by the addition of Milli-Q water. The analytical precision and accuracy for trace elements are similar to those of Liu et al. (2008).

### 3.4. Nd and Sr isotopes

The abundances of Sr and Nd isotopes in samples of dacitic host rocks and apatite grains from massive ore and veinlets that cross-cut altered host rocks were determined at the Key Laboratory of Mineralogy and Metallogeny, Guangzhou Institute of Geochemistry, Chinese Academy of Sciences, Guangzhou, China. The analytical data acquired are provided in Supplementary Table 3. Samples for Sr–Nd isotopic analysis were dissolved in Teflon bombs using a HF + $HNO_3$ acid mixture. Strontium and Nd were separated using conventional ion exchange procedures and measured using a Neptune Plus MC-ICP-MS. Procedure blanks of the total chemical treatment were at the level of<1 ng for Nd and Sr. During the period of laboratory analysis, measurements of NIST SRM- Sr standard yielded a $^{87}Sr/^{86}Sr$ ratio of 0.710250 ± 0.000030 (2σ), and the JNdi-1 Nd standard yielded a $^{143}Nd/^{144}Nd$ ratio of 0.512115 ± 0.000004 (2σ).

## 4. Results

### 4.1. Apatite textures, chemistry and inclusions

The major and minor element compositions of apatite grains, including Ca, P, F, Cl, S, Na, Fe, Sr, Mn, Si, Y, La and Ce, are reported in Supplementary Table 1. Spot analyses and core-to-rim transects were conducted by EPMA to assess chemical zonation within and among apatite grains (Fig. 5). All apatite grains are euhedral to subhedral. Back scattered electron (BSE) imaging and EPMA analyses revealed two distinct populations of apatite grains in samples from Chah-Gaz. Unzoned apatite grains disseminated within, and coeval with, massive magnetite are dominantly fluorapatite (Fig. 5A, B). However, the BSE images reveal that some fluorapatite grains coeval with massive magnetite exhibit subtle chemical zonation and the presence of secondary monazite and thorite and, possibly, quartz (Fig. 5C). Apatite grains coeval with massive magnetite plot near the F-rich corner of the F-Cl-OH ternary (Fig. 6A).

Petrographic observations and BSE images reveal a second type of apatite present within veinlets that cut the host rocks. The veinlet-hosted, late-stage apatite grains are chemically heterogeneous, where in individual grains have F-rich cores and F-depleted rims and are associated with thorite ± zircon ± xenotime ± monazite (Fig. 5D & E). Fluorine-rich apatite cores are characterized by Cl/F ratios up to 0.04 and a F/OH ratio that ranges from 1.6 to 3.6. The F-depleted rims of apatite grains yield ratios of Cl/F, F/OH and Cl/OH that range, respectively, from 0.06 to 0.13, 1.9 to 6.4. and 0.15 to 0.79 (Supplementary Table 1). A BSE image and data from a core-to-rim analytical transect reveal that the veinlet-hosted apatite exhibits a decrease from a F-rich core with about 2.5 wt% F to a F-depleted rim that contains about 1.6 wt % F (Fig. 6). In that grain, which is representative of all veinlet-hosted apatite grains, the F/Cl ratio decreases from ca. 313 for the core to 8 for the rim. The abundances of Ca and P in zoned, veinlet-hosted apatite grains sum to about 94% wt. % in the F-rich core of apatite grains relative to the rims of F-depleted apatite where CaO + $P_2O_5$ sum to about 91 wt% (Fig. 6C). The fluorapatite domains in veinlet-hosted apatite grains are systematically enriched in S, Na and Sr relative to F-depleted domains (Fig. 6d). The core of veinlet-hosted apatite grainsplot near the F-rich corner of the F-Cl-OH ternary, whereas the rim of those apatite grains plots near the F-rich corner of the ternary further from that apex toward the Cl-OH binary (Fig. 7A).

The REE abundances of both types of apatite (i.e., apatite coeval with massive magnetite, and apatite in late-stage veinlets) are reported in Supplementary Table 1 and presented graphically in Fig. 8. Apatite grains in the massive ore bodies (i.e., apatite coeval with massive magnetite) and veinlet-hosted apatite both exhibit a strong negative Eu anomaly, yielding Eu/Eu* anomalies of 0.14 to 0.38 and 0.13 to 0.23, respectively (Fig. 8). The chondrite normalized REE patterns for apatite coeval with magnetite from the main ore body indicate that apatite is somewhat enriched in LREE relative to HREE, with with a (La/Yb)cn = 1.45–1.67 (Fig. 8). On the contrary, the chondrite normalized REE patterns for veinlet-hosted apatite reveal an almost flat REE pattern (Fig. 7). The F–depleted apatite rims in veinlets that cut the host rocks have (La/Yb)cn = 0.89–0.97, whereas the F-enriched cores of veinlet-hosted apatite grains have (La/Yb) cn = 0.94–1.06.

### 4.2. The whole rock geochemistry of volcanic host rocks and gabbro

The major element oxide abundances for whole-rock samples of dacitic-rhyodacitic host rocks indicate a narrow range for $SiO_2$ (68.5–68.7 wt%) and $Al_2O_3$ (13.8–14.5 wt%), whereas the concentrations of $K_2O$ (5.9–6.8 wt%) and $Na_2O$ (0.3–1.7 wt%) exhibit more variability (Supplementary Table 2). On a total alkali–silica (TAS)

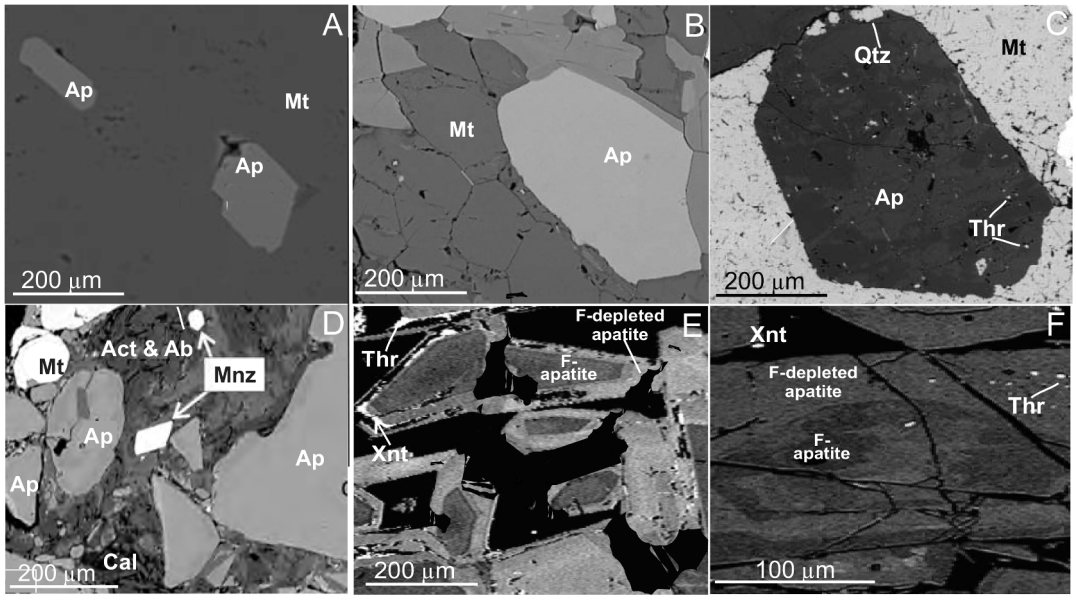


**Fig. 5.** The BSE images of (A) and (B) unzoned and (C) subtle chemical zonation in the fluorapatite grains coeval with massive magnetite; (D) Individual apatite grains related to altered host rock with thorite ± zircon ± xenotime ± monazite; (E and F) F-rich cores and F-depleted rims apatite related to altered host rock.

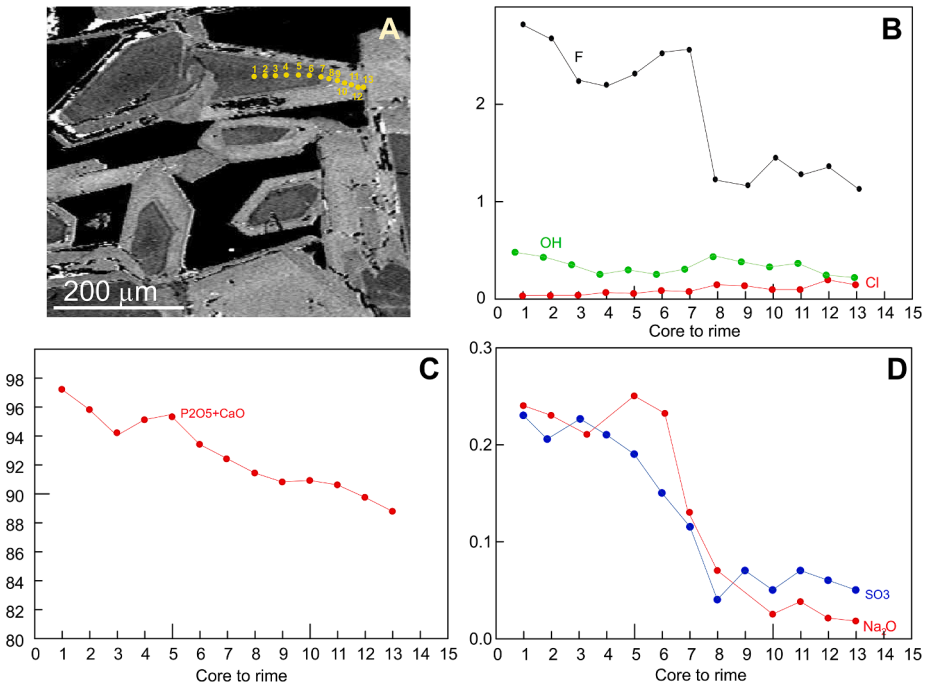


**Fig. 6.** (A) Apatite related to veinlet within the atered host rocks with dark and light domains showing the location of the analyzed points; (B) Traverse showing the F, Cl and OH atomic proportions represented as percentages (%); (C) Traverse showing the $P_2O5 + CaO$ represented as percentages (%); (D) Traverse showing the $SO_3$ and $Na_2O$ represented as percentages (%).

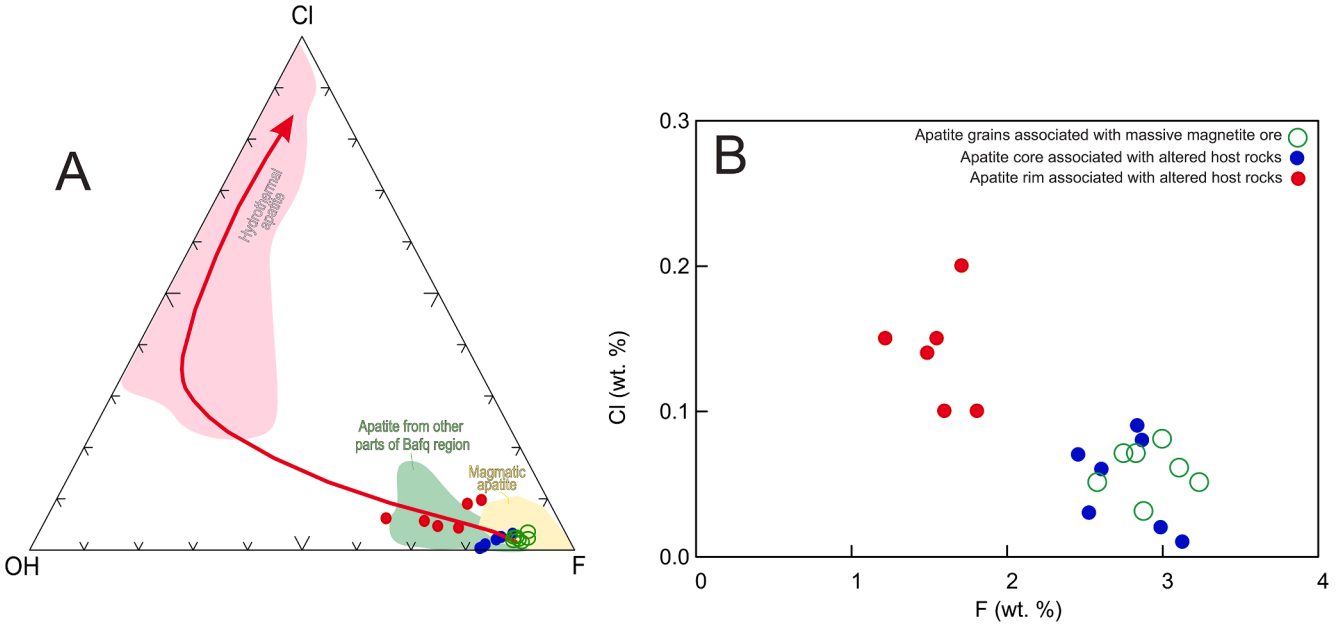


**Fig. 7.** (A) Ternary plot of the halogen content in apatite in terms of the F-Cl-OH atomic proportions. Fields are based on the Carmen, Fresia and Mariela EPMA data from Palma et al., 2019), in which F-rich compositions represent a magmatic, primary apatite and Cl- and OH-apatite hydrothermal/metasomatic apatite; (B) Divariant plot of F and Cl concentrations (wt%). The plot shows a negative correspondence between F and Cl. Apatite analyses (massive magnetite ore: open green circles; altered host rock: blue circle is F-rich core and red circle is F-depleted rims).

diagram, the host rocks are enriched in alkali elements ($Na_2O + K_2O$ = 7.3 wt%) and plot within the fields for dacite and rhyodacite (cf. Le Bas et al., 1986)) (Fig. 9A). Dacite samples have elevated $K_2O$ contents of ~ 5.9 to 7.1 wt%, similar to data reported for shoshonitic rocks (Fig. 9C) and volcanic arc granites (Fig. 9D) (Peccerillo and Taylor, 1976). Chondrite-normalized REE patterns of dacite are more enriched in LREEs relative to HREEs, yielding a (La/Yb(cn) ratio of 9.9–10.2 and Eu/Eu* anomalies of 0.46–0.70 (Fig. 10). Gabbro-diorite samples display a narrow range of $SiO_2$ (57.8–59.6 wt%) and $Al_2O_3$ (13.8–14.2 wt%). These rocks have low $K_2O$ (0.96–1.2 wt%) but high $Na_2O$ (6.86–7.01 wt %) contents, enriched in alkali elements ($Na_2O + K_2O$ = 7.8–9.0 wt%) and plot within the trachyandesite field on a TAS diagram (Fig. 9A; after Le Bas et al., 1986). The A/CNK ratios for alkaline gabbro-diorite rocks are 1.15–1.30, implying a relatively peraluminous affinity (Fig. 9B). They are enriched in $Na_2O$, with $K_2O/Na_2O < 1$ and plot in the tholeiitic to somewhat calc-alkaline and within-plate fields in $K_2O$–silica and Y +

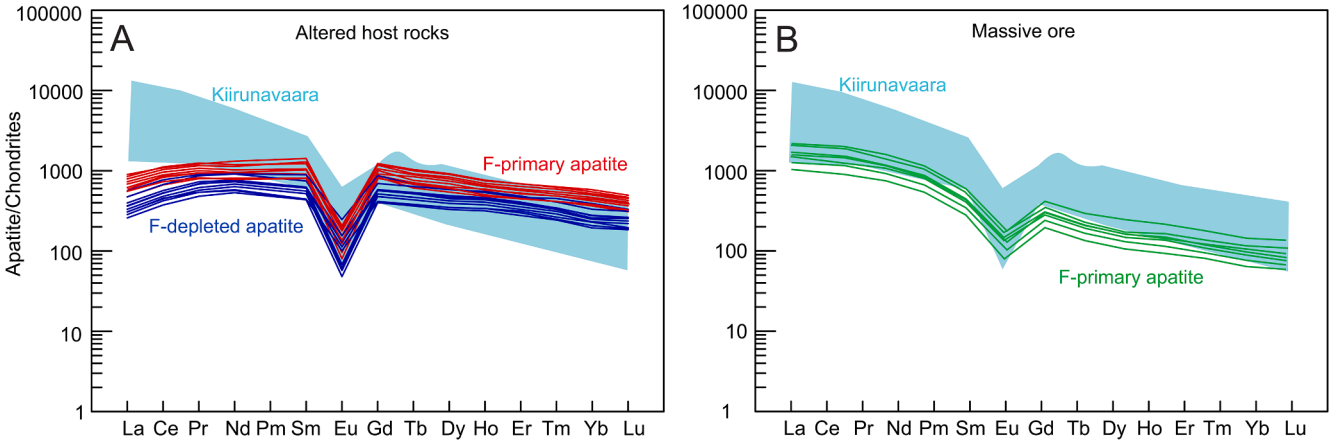


**Fig. 8.** REE patterns for each apatite type or domain from (A) cores and rims of apatite from veinlets within the altered host rock, (B) apatite associated with massive magnetite ore.

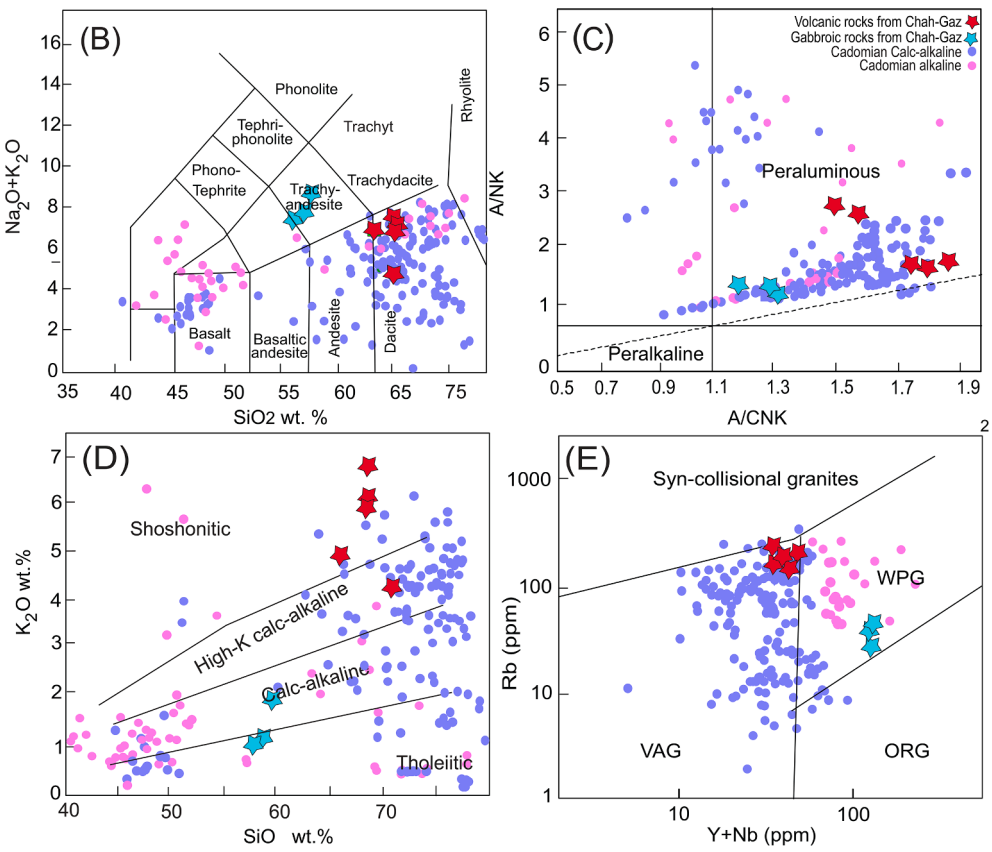


**Fig. 9.** Geochemical data for and classifications of Chah-Gaz volcanic host rocks. (A) The total alkali–silica diagram (Lebas et al., 1986); (B) ANK (molar $Al_2O_3/(Na_2O + K_2O)$) *vs* A/CNK (molar $Al_2O_3/(CaO + Na_2O + K_2O)$) diagram; (C) $SiO_2$ *vs* $K_2O$ diagram (Peccerillo and Taylor, 1976) and (D) Rb *vs* Y + Nb diagrams (Pearce et al., 1984). Data for magmatic rocks are from Badr et al., 2013; Balaghi et al., 2014; Moghadam et al., 2015, 2016 2017a), and data for Cadomian exotic blocks within salt domes is from Asadi et al., (2020). Data for NE and Central Iran alkaline mafic rocks are from (Balaghi et al., 2010; Veiskarami et al., 2019; Sepidbar et al., 2020). Data for Saghand rocks are from (Ramezani and Tucker, 2003).

Nb *vs*. Rb (Pearce et al., 1984) diagrams, respectively (Fig. 9C and D). Chondrite-normalized rare earth element (REE) patterns (Sun and McDonough, 1989) for gabbro-diorite show that they are somewhat enriched in LREEs relative to HREEs, with $La_N/Yb_N$ ratio of 1.9–2.4, without Eu anomalies (Eu/Eu* = 1.1–1.2) (Fig. 10).

### 4.3. Strontium and Nd isotopes

Whole rock Sm-Nd isotopic data for ores (two types of apatite), host rocks (two dacites) and gabbro (two samples) from Chah-Gaz are presented in Fig. 10 and Supplementary Table 3. Values of εNdi were calculated based on an age of 534 Ma for zircon grains in the host rocks (this study) and gabbros obtained by Sepidbar et al., Unpublished for comparison. The $^{87}Rb/^{86}Sr$ ratios of Chah-Gaz dacitic rocks range from 0.54 to 0.63. The isotopic data yield initial εNd(t) and $(^{87}Sr/^{86}Sr)_{(i)}$ values of −5.5 to −7.6 and 0.7168 to 0.7104, respectively, with depleted mantle model ages ($T_{DM}$) of ~ 1.6–1.8 Ga. The $(^{87}Sr/^{86}Sr)_{(i)}$ values for the dacitic-rhyodacitic host rocks are highly variable, although they have a restricted range of negative εNd(*t*) values. The Chah-Gaz gabbro-diorite yielded a $^{87}Rb/^{86}Sr$ ratio of 0.35 to 0.80. The gabbro-diorite samples yielded a positive initial εNd(t) and $(^{87}Sr/^{86}Sr)_{(i)}$ values of + 1.3 to + 2.7 and 0.7052 to 0.7064, respectively, with $T_{DM}$ of ~ 0.7–1.1 Ga.

Apatite from massive magnetite ore and veinlets that cross-cut altered host rocks contains 171–749 ppm Sr and < 0.1 lg/g Rb) and, therefore, low Rb/Sr ratios. Hence, only the $^{87}Sr/^{86}Sr$ ratio was

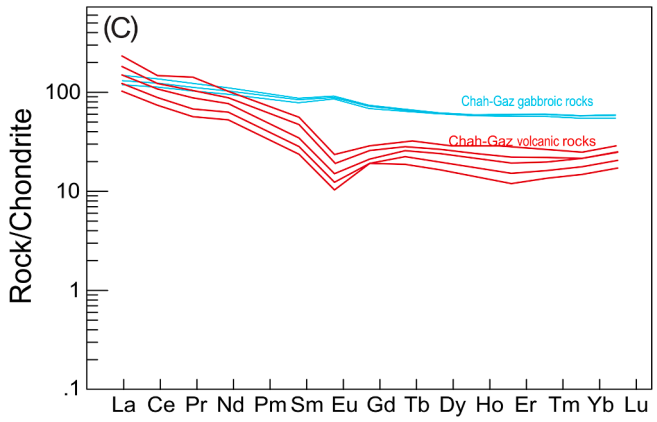


**Fig. 10.** Chondrite-normalized REE patterns (right) for Chah-Gaz and Mishdovan Cadomian dacitic rocks. Chondrite- normalized values are taken from (Sun and McDonough, 1989).

measured. The Sm, Nd, and Sr concentrations and isotope ratios are reported in Supplementary Table 2. The analyzed apatite grains yield a $^{147}Sm/^{144}Nd$ ratio ranging from 0.1120 to 0.1329 for F-rich apatite, 0.1284 to 0.1501 for F-depleted apatite. In addition, F-rich apatite yields $^{143}Nd/^{144}Nd$ and $^{87}Sr/^{86}Sr$ ratios ranging from 0.512590 to 0.512904 and 0.70322 to 0.70472, respectively, whereas F-depleted apatites yield $^{143}Nd/^{144}Nd$ and $^{87}Sr/^{86}Sr$ ratios of 0.51226–0.51275 and 0.70421–0.70590, respectively (Supplementary Table 3). Analyses of F-rich apatite cores yielded εNd values that range from + 5.7 and + 6.8, whereas F-depleted apatite rims yielded εNd values that range from −0.4 to + 3.9 (Fig. 11). Gabbro-diorite from the Chah-Gaz complex yielded more juvenile (mantle-derived) isotopic compositions than the calc-alkaline dacites and similar isotopic compositions with apatite rim and core.

## 5. Discussion

### 5.1. Ore-fluid source region inferred from trace elements and Nd -Sr isotopes

The Chah-Gaz dacitic host rocks exhibit strong an arc-like geochemical signature similar to I-type igneous rocks (Fig. 9). The Chah-Gaz dacites plot in the VAG and continental magmatic arc-related rocks in Rb *vs* [Y + Nb] (Fig. 9D). The dacitic host rocks are enriched in

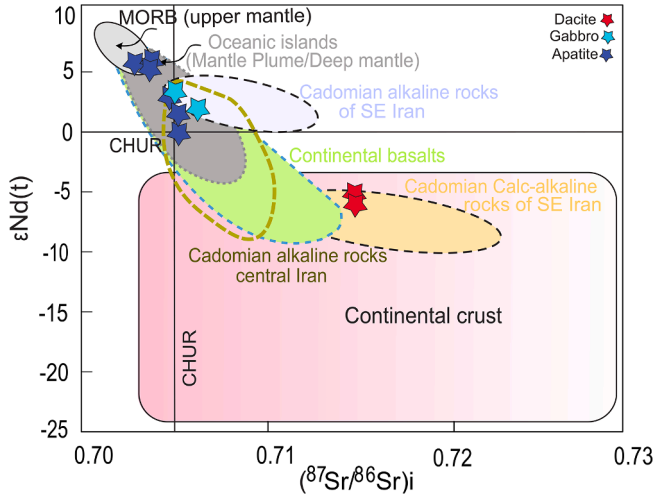


**Fig. 11.** εNd *vs* $^{87}Sr/^{86}Sr$ diagram for the Chah-Gaz Cadomian dacitic rocks. Bulk-rock Nd isotope data for Cadomian magmatic rocks are from Sepidbar et al. (2020) and references therein.

LREEs, Rb, Ba, Th, U, Pb, and K, and depleted in Nb and Ti, which are all salient geochemical features for igneous rocks formed in an active continental arc environment (Pearce and Peate, 1995; Baier et al. 2008). The Chah-Gaz gabbro-diorite rocks are enriched in LREEs, with or without depletions in Nb (Fig. 10). These rocks have high $Na_2O$ (6.86–7.01 wt%) and FeO/MgO ratios (3.9–4.2), but low $Al_2O_3$ (13.8–14.2 wt%), Cr (15–24 ppm), Co (30.1–41.0 ppm) and Ni (7.0–8.3 ppm) contents, similar to rocks formed in the intraplate setting. Such geochemical signatures indicate that these arc-related and intraplate magmas formed in subduction-related rift zones or continental back-arc settings (Fig. 9D).

The εNdi values for apatite from the ore bodies range from ~ 0 to ~ 5 and are distinctly different than the negative εNdi values for the dacitic host rocks that overlap the fields for continental crust and Cadomian calc-alkaline rocks of southeast Iran (Fig. 11). Apatite is ubiquitously intergrown with magnetite in the ore bodies, which is consistent with co-crystallization of the two minerals (e.g., La Cruz et al., 2020). Consequently, the whole rocks Sm-Nd signature of apatite is a proxy for the source of the ore fluid from which both apatite and magnetite crystallized. The whole rock Sm-Nd results of the dacitic host rocks indicate a source region related to Cadomian crust, whereas Sm-Nd concenrations of the gabbroic rocks indicate a mantle source region.

The εNdi values for apatite grains from the ore samples show a stronger influence of a depleted mantle source, comparable to the whole rock Sm-Nd, similar to those of gabbroic rocks (Fig. 11). Together, both isotope systems point towards a depleted mantle source influence for the ores, in contrast to a dominantly crustal influence for metavolcanic host rocks. Westhues et al. (2016; 2017a; 2017b) reported similar observations for igneous host rocks and ore in the Kiruna IOA district, Sweden, and used those data along with zircon Hf and O isotopic data to conclude that a magmatic-hydrothermal fluid evolved from mantle-derived silicate magma was responsible for IOA mineralization in the Kiruna district. Those authors concluded that the ore at Kiruna could not have formed from an immiscible Fe-rich liquid.

The Sm-Nd compositions of F-depleted apatite in the Chah-Gaz ore samples are statistically different from those of the F-rich apatite in the massive magnetite ore bodies. This is similar to studies of apatite from the Taocun IOA deposit (Zeng et al., 2016) and Yinachang Fe-Cu-REE deposit (Zhao et al., 2015), both in China. Those authors used in situ LA-MC-ICP-MS for measure Sm and Nd isotope abundances in unaltered and altered domains within individual apatite grains and concluded that that the metasomatic fluids responsible for apatite alteration were more enriched in radiogenic Sr and were more likely to have a greater contribution from sedimentary rocks due to fluid circulation.

The F-rich apatite from Chah-Gaz shows higher and narrow εNd values of + 5.8 to + 6.7, and the lower initial $^{87}Sr/^{86}Sr$ values of 0.70322 to 0.70472 than those of the F-depleted apatite (-0.4 to + 3.9 and 0.70421 to 0.70590, respectively), consistent with role of a crustal influence or hydrothermal fluids related to secondary metasomatic and/or coupled dissolution-reprecipitation events for the formation of F-depleted rims.

### 5.2. Implication for magmatic and hydrothermal ore forming processes at Chah-Gaz

The partitioning of F, Cl and OH between apatite and silicate melt, and apatite and hydrothermal fluid, depends on melt and/or fluid composition, temperature, pressure, oxygen fugacity, and the existence of additional phases that compete for F and Cl (Zhu and Sverjensky, 1991). Apatite that crystallizes from silicate melt is ubiquitously fluorapatite and in the absence of co-crystallizing biotite and/or amphibole, is the dominant sink for fluorine during magma evolution (Zhu and Sverjensky, 1991). Apatite in felsic-intermediate igneous rocks shows a limited F-OH-Cl compositional range with XF-apatite 50–100%, XOH-apatite 0–50% and XCl-apatite < 20% (Piccoli and Candela, 2002). Apatite is a liquidus, or near-liquidus, phase in intermediate silicate

melts and the Cl/F ratio of the melt increases during apatite fractionation. If the melt reaches volatile saturation and exsolves a magmatic volatile phase, Cl is preferentially partitioned into the volatile phase (Piccoli and Candela, 2002; Kiprianov and Karpukhina, 2006; Kiprianov, 2006). The data reported here for apatite samples from the Chah-Gaz ore body reveal a limited F-OH-Cl compositional range consistent with fluorapatite (>2.5 wt% F) as a primary phase coeval with magnetite in the massive ore bodies (Fig. 7A), whereas apatite grains disseminated in the host rocks contain fluorapatite cores and F-depleted rims (Fig. 7). The systematic zonation of fluorine is best explained by coupled dissolution-reprecipitation of apatite in the presence of a syn- or post-mineralization F-poor hydrothermal fluid. The occurrence of F-depleted apatite rims and fracture fillings are consistent with F-depletion by syn to post-mineralization hydrothermal processes. It is plausible that the F-depleted rims formed during the mineralization event as the ore fluid cooled and the F concentration of the ore fluid was depleted by sequestration of F into the original precipitating apatite during *syn*-mineralization hydrothermal alteration stage. These processes are also evidenced by the occurrence of fine-grained Cl-OH-apatite in Chadormalu (Heidarian et al., 2018) and Esfordi (Bonyadi et al., 2011). In samples from Chah-Gaz, further evidence for coupled dissolution-reprecipitation reactions includes the presence of apatite with an acicular texture (Fig. 3E) and the presence of monazite and xenotime inclusions (Fig. 5) (Sidder et al., 1993; Bargossi et al., 1999; Harlov et al., 2002; Piccoli and Candela, 2002; Daliran et al., 2010; Jonsson et al., 2016; Betkowski et al., 2016; La Cruz et al., 2019; Palma et al., 2019). The depletion of the LREE in F-depleted apatite rims, in addition to the relative Th and U depletion compared to other domains within apatite grains from the Chah-Gaz deposits (Supplementary Table 1) are also consistent with fluid-mediated coupled dissolution-reprecipitation of apatite that liberated the LREE, Th, U, and P, and resulted in crystallization of monazite and xenotime inclusions. Unzoned fluorapatite apatite grains from the Chah-Gaz massive ores contain a homogeneous distribution of Th and U and no LREE depletion (Fig. 8B). Kusebauch et al. (2015) reported that synthetic F-depleted apatite can be substituted by the formation of porous metasomatized apatite or a solid solution between F-OH-Cl-apatite due to interaction with hydrothermal fluids (KOH, NaCl and NaF) at 400–700 °C and 0.2 GPa. Therefore, formation of apatite with porous rims and pristine, porosity-free core at Chah-Gaz can be explained by interaction with saline hydrothermal fluids. The relatively constant Sr and Nd data in both generations of apatite are consistent with superimposed, episodic hydrothermal fluids from the same, evolving, magmatic-hydrothermal system as reported by Del Real et al. (2021) for the Candelaria iron oxide - copper - gold (IOCG) system, Chile.

Petrographic and field observations that include alteration zones such as sodic-calcic, potassic, magnesium, silicic and carbonatization with abundant actinolite, epidote, minor albite and occasionally scapolite supports the involvement of hydrothermal fluids in the evolution of the Chah-Gaz IOA deposits. Late-stage or post-mineralization re-equilibration of apatite with hydrothermal fluid is also evinced by the presence of magnetite-rich veinlets that crosscut the massive ore bodies. Treloar and Colley (1996) suggested that the presence of mm-thick magnetite and epidote veinlets, and apatite and actinolite crystals in these deposits are indicative of a low viscosity hydrothermal fluid. Ziapour et al. (2021) reported oxygen and sulfur isotopic data for magnetite and associated pyrite and proposed that an iron-rich magmatic-hydrothermal fluid generated the massive magnetite-rich ore bodies in the Chah-Gaz IOA deposit. The data presented here are consistent with Ziapour et al. (2021) and indicate formation of the apatite within the massive magnetite-rich ore bodies and veinlets that cross cut the the altered host rocks in the Chahgaz deposit formed by a hypogene iron-rich magmatic-hydrothermal fluid.

### 5.3. Sulfur in Chah-Gaz apatite

The positive relationship between S and Na in veinlet-hosted apatite and apatite disseminated in the host rocks (Fig. 6d) is consistent with the coupled substitution of $(SO_4)^{2-} + Na^{+} = (PO_4)^{3-} + Ca^{2+}$ during apatite crystallization. Konecke et al. (2017; 2019) demonstrated experimentally using in situ sulfur X-ray absorption near edge structure (S-XANES) analysis of apatite crystallized experimentally at controlled $fO_2$ conditions that apatite incorporates $S^{6+} > S^{2-} \gg S^{4+}$ depending on $fO_2$. The S-enrichment of the fluorapatite cores at Chah-Gaz is consistent with apatite growth from oxidized silicate melt or high-temperature magmatic-hydrothermal fluid. Considering that the sulfur in oxidized silicate melt is dominantly $S^{6+}$, whereas sulfur is dominantly $S^{4+}$ in hydrothermal fluid, the S-rich nature of fluorapatite plausibly records fluorapatite crystallization from oxidized silicate melt. The sharp decrease of S, F and Na at the interface of the apatite core and rim (Fig. 6A) is consistent with coupled dissolution-reprecipitation of primary fluorapatite in the presence of Cl-bearing hydrothermal fluid that resulted in the euhedral F-poor overgrowths and secondary monazite and xenotime.

### 5.4. The role of fluid-apatite interaction mechanism

Fluid-mineral interaction triggered by the penetration of a hydrothermal fluid of a specific composition that is in disequilibrium with apatite, or a change of temperature and/or pressure, can cause the dissolution of the primary F-apatite, such that the resulting fluid could become supersaturated in certain components (e.g., U, Th and REEs; Putnis, 2002; 2009) or REE were leached from apatite, resulting in precipitation of monazite and xenotime. In apatite from veinlets within the Chah-Gaz altered host rocks, fluid-apatite interaction was limited and controlled by the formation of F-depleted-apatite rims, with cores typically fresh, signifying a low fluid/apatite interaction. LREEs are more readily mobilized by hydrothermal fluids than HREEs (Reed et al., 2000), particularly at high temperatures and by low-pH fluids (Williams-Jones et al., 2012). Therefore, LREE possibly will have been successfully leached from primary F apatite by F-depleted hydrothermal fluids, allowed monazite formation, and replacement of F apatite by Cl- and Cl-OH apatite. Besides, the fluid-resolved reaction of monazite and xenotime with the surrounding silicate minerals is able to yield allanite as seen in places together with apatite from veinlets within the Chah-Gaz altered host rocks.

In summary, the presence of monazite and xenotime inclusions in Chah-Gaz apatite are explained by higher initial Y + REEs concentration (>0.2–0.3 wt%) of primary fluorapatite that reacted with hydrothremal fluid either during formation of the massive ore bodies or post-mineralization. Fluorapatite from the Chah-Gaz massive ores has high εNd (5.8–6.7) and low initial $^{87}Sr/^{86}Sr$ isotopic values (0.7032–0.7047) (Supplementary Table 3; Fig. 11), which is consistent with a mantle origin of gabbroic rocks (Fig. 11), with minimal crustal contribution. These values are also in agreement with the textural and geochemical magmatic signature of unaltered fluorapatite. In contrast, apatite from veinlets within the altered host rocks has lower εNd values (-0.4 to + 3.9) and higher $^{87}Sr/^{86}Sr$ (0.7042 to 0.7059), possibly as a result of fluid-rock interaction with crustal fluids enriched in radiogenic Sr. Similar conclusions have been reported for apatite from IOA deposits in the Chilean iron belt (Palma et al., 2019), and the Yinachang Fe-Cu-REE deposit, China (Zhao et al., 2015) and the Taocun IOA deposit, China (Zeng et al., 2016).

### 5.5. A model for the formation of the Chah-Gaz IOA deposit

The geochemical data reported here for apatite from the Chah-Gaz IOA deposit are consistent with a magmatic origin with little or no crustal contamination. The data are consistent with Ziapour et al. (2021) who reported oxygen isotope data for magnetite from Chah-Gaz that

fingerprint a magmatic source reservoir for oxygen. Those authors also report that the abundances of minor elements in magnetite (e.g., Ti, V, Al, Mn) overlap compositions reported for igneous and high-temperature magmatic-hydrothermal magnetite. Ziapour et al. (2021) concluded that the massive magnetite bodies at Chah-Gaz formed by a combination of igneous and magmatic-hydrothermal processes as originally described by Knipping et al. (2015a). Briefly, the genetic model developed by Knipping et al. (2015a) invokes crystallization of magnetite and fluorapatite from an oxidized, intermediate composition silicate melt such as andesite, followed by exsolution of a magmatic-hydrothermal fluid from the melt where the fluid bubbles nucleate and grow on magnetite and apatite crystal faces and form a magnetite-apatite-fluid suspension. The fluid-crystal suspension is less dense than the surrounding melt and will ascend buoyantly through the magma and evolve from the magma along permeable structures such as faults in the superjacent environment. Deposition of magnetite and fluorapatite occurs in faults when the proportion of magnetite and apatite in the suspension exceed about 40 vol%, depending on the density (i.e., salinity) of the fluid (Knipping et al., 2015a, 2019). The S-enrichment of primary fluorapatite at Chah-Gaz is consistent with growth from oxidized silicate melt (cf. Konecke et al., 2017; 2019). The F-poor rims on primary fluorapatite reported here are consistent with Ziapour et al. (2021) who reported the presence of vesicles within the primary massive magnetite ore bodies and magnetite rims that record local dissolution and reprecipitation of magnetite during emplacement of the ore fluid suspension.

## 6. Conclusions

The Chah-Gaz ore deposit is one of the largest IOA deposits in Bafq district. The deposit is hosted in calc-alkaline and alkaline igneous rocks that range from granite to diorite and rhyolite to rhyodacite as well as alkaling gabbr-dioritic rocks that are increasingly altered with proximity to the magnetite-rich ore bodies, and display replacement textures. The characteristics of the Chah-Gaz deposit are consistent with Kiruna-type iron oxide- apatite (IOA) deposits globally, including (i) several types of hydrothermal alteration such as sodic-calcic, potassic, magnesium, silicic and carbonatization, (ii) calc-alkaline affinities of igneous rocks associated to mineralization, (iii) chemical composition of magnetite, and (iv) low sulfide contents of ores. The geochemical and tectono-magmatic investigations in this deposit indicate a calc-alkaline and active continental-margin arc setting for felsic host rocks in relation to subduction of Proto-Tethyan oceanic crust beneath the Central Iranian microcontinent in the Early Cambrian followed by emplacement of diabasic dykes in a back-arc basin. Primary fluorapatite is consistent with growth from silicate melt, whereas F-depleted apatite rims indicate coupled dissolution-reprecipitation in the presence of hydrothermal fluid. The data for apatite are consistent with previously reported $\delta^{18}O$ values for for coeval magnetite in the massive ore bodies that indicate a silicate magma source reservoir for oxygen. The data are consistent with initial growth of magnetite from silicate melt, subsequent degassing of the melt and formation of a magnetite-apatite fluid suspention that ascended along faults to form the massive ore bodies. Ziapour et al. (2021) proposed that a decrease of oxygen fugacity and increase of sulfur fugacity during emplacement of the ore bodies led to deposition of late-stage pyrite, which is consistent with the S-rich nature of primary fluorapatite and S- and F-depleted late-stage rims.

## Declaration of Competing Interest

The authors declare that they have no known competing financial interests or personal relationships that could have appeared to influence the work reported in this paper.

## Acknowledgements

This is Pos-Doc research contribution #98019789 funded by Iran National Science Foundation. We thank to Prof. Franco Pirajno, editor-in-chief, and two anonymous reviewers for the positive comments and suggestions, improving the manuscript greatly. F. Sepidbar acknowledges support from Damghan University for assistance during the field work. ACS acknowledges funding from NSF EAR 1924142.

## Appendix A. Supplementary data

Supplementary data to this article can be found online at https://doi.org/10.1016/j.oregeorev.2021.104599.

## References

Baier, J., Audétat, A., Keppler, H., 2008. The origin of the negative niobium-tantalum anomaly in subduction zone magmas. Earth Planet. Sci. Lett. 267 (1-2), 290–300.
Bargossi, G.M., Del Moro, A., Ferrari, M., Gasparotto, G., Mordenti, A., Rottura, A., Tateo, F., 1999. Caratterizzazione petrografico-geochimica e significato dell'associazione monzogranito- inclusi femici microgranulari della Vetta di Cima d'Asta (Alpi Meridionali). Mineral. Petrog. Acta 42, 155–179.
Barton, M.D., Johnson, D.A. (2004) Footprints of Fe-oxide (-Cu-Au) systems. University of Western Australia Special Publication, 33, 112–116.
Betkowski, V., Harlov, D., Rakovan, J., 2016. Hydrothermal mineral replacement reactions for an apatite-monazite assemblage in alkali-rich fluids at 300–600 _C and 100 MPa. Am. Mineral. 101, 2620–2637.
Bonyadi, Z., Davidson, G.J., Mehrabi, B., Meffre, S., Ghazban, F., 2011. Significance of apatite REE depletion and monazite inclusions in the brecciated Se-Chahun iron oxide-apatite deposit, Bafq district, Iran: Insights from paragenesis and geochemistry. Chem. Geol. 281 (3-4), 253–269. https://doi.org/10.1016/j.chemgeo.2010.12.013.
Daliran, F., Stosch, H.G., Williams, P., Jamli, H., Dorri, M.B., 2010. Early Cambrian Iron Oxide-Apatite-REE (U) Deposits of the Bafq District, East-Central Iran. In Exploring for Iron oxide copper-gold deposits: Canada and Global analogues (Eds. L. Corriveau, H. Mumin). Geol. Assoc. Canada Short Course Notes 20, 143–155.
Dare, S., Barnes, S.J., Beaudoin, G., 2015. Did the massive magnetite "lava flows" of El Laco (Chile) form by magmatic or hydrothermal processes? New constraints from magnetite composition LA-ICP-MS. Miner Deposita 50, 607.
Del Real, I., Reich, M., Simon, A.C., Deditius, A., Barra, F., Rodríguez-Mustafa, M.A., Thompson, J.F.H., Roberts, M.P., Formation of giant iron oxide - copper - gold deposits by superimposed, episodic hydrothermal events. Nature Communications Earth & Environment https://doi.org/10.1038/s43247-021-00265-w.
Gao, S., Liu, X., Yuan, H., Hattendorf, B., Günther, D., Chen, L., Hu, S., 2002. Determination of Forty Two Major and Trace Elements in USGS and NIST SRM Glasses by Laser Ablation-Inductively Coupled Plasma-Mass Spectrometry. Geostandards and Geoanalytical Research 26 (2), 181–196. https://doi.org/10.1111/j.1751-908x.2002.tb00886.x.
Ghorbani, M., 2013. The Economic Geology of Iran. Mineral Deposits and Natural Resources.
Haghipour, A., Pelissier, G., 1977, Geology of the Saghand Sector, *in* Haghipour, A., Valeh, N., Pelissier, G., and Davoudzadeh, M., editors, Explanatory Text of the Ardekan Quadrangle Map: Geological Survey of Iran, H8, p. 10–68.
Hansen, E.C., Harlov, D.E. (2007) Whole-rock, phosphate, and silicate compositional trends across an amphibolite-to granulite- facies transition, Tamil Nadu, India. J. Petrol. 48, 1641–1680.
Harlov, D.E., Andersson, U.B., Förster, H.-J., Nyström, J.O., Dulski, P., Broman, C., 2002. Apatite-monazite relations in the Kiirunavaara magnetite- apatite ore, Northern Sweden. Chem. Geol. 191 (1-3), 47–72.
Harlov, D.E., Forster, H.J., 2003. Fluid-induced nucleation of (Y+REE)-phosphate minerals within apatite: nature and experiment Part II. Fluorapatite. Am. Min. 88, 1209–1229.
Harlov, D.E., Wirth, R., Förster, H.-J., 2005. An experimental study of dissolution–reprecipitation in fluorapatite: fluid infiltration and the formation of monazite. Contrib. Mineral. Petrol. 150 (3), 268–286.
Heidarian, H., Lentz, D.R., Alirezaei, S., McFarlane, C.R.M., Peighambari, S., 2018. Multiple stage ore formation in the chadormalu iron deposit, Bafq Metallogenic Province, Central Iran: evidence from BSE imaging and apatite EPMA and LA-ICP-MS U-Pb geochronology. Minerals 8, 87. https://doi.org/10.3390/min8030087.
Hou, T., Charlier, B., Holtz, F., Veksler, I., Zhang, Z., Thomas, R., Namur, O., 2018. Immiscible hydrous Fe–Ca–P melt and the origin of iron oxide-apatite ore deposits. Nat. Commun. 9, 1415.
Hushmandzadeh, A., 1969. Metamorphisme et granitisation du massif Chapedony (Iran Central): These. Universite Scientifique et Medicale de Grenoble, France, p. 242.
Jonsson, E., Harlov, D.E., Majka, J., Hogdahl, K., Persson-, N.K., 2016. Fluorapatite-monazite-allanite relations in the Grangesberg apatite-iron oxide ore district, Bergslagen, Sweden. Am. Min. 101, 1769–1782.
Kim, Y., Koecke, B., Fiege, B., Simon, A., Becker, U., 2017. An ab-initio study of the energetics and geometry of sulfide, sulfite and sulfate incorporation in apatite; the thermodinamic basis for using this system as an oxybarometer. Am. Min. 102, 1646–1656.
Kiprianov, A.A., 2006. Regular trends in uptake of halogens by alkali silicate glasses containing two glass-forming components. Russ. J. App. Chem. 79, 20–28.
Kiprianov, A.A., Karpukhina, N.G., 2006. Oxyhalide silicate glasses. Glass Phys. Chem. 32, 1–27.

Knipping, J.L., Bilenker, L.D., Simon, A.C., Reich, M., Barra, F., Deditius, A.P., Lundstrom, C., Bindeman, I., Munizaga, R. (2015a) Giant Kiruna-type deposits form by efficient flotation of magmatic magnetite suspensions. Geology 43, 591–594.
Knipping, J.L., Bilenker, L.D., Simon, A.C., Reich, M., Barra, F., Deditius, A.P., Wälle, M., Heinrich, C.A., Holtz, F., Munizaga, R., 2015b. Trace elements in magnetite from massive iron oxide-apatite deposits indicate a combined formation by igneous and magmatic-hydrothermal processes. Geochim. Cosmochim. Acta 171, 15–38.
Knipping, J., Webster, J.D., Simon, A.C., Holtz, F., 2019. Accumulation of magnetite by flotation on bubbles during decompression of silicate magma. Sci. Rep. 9, 3852.
Konecke, B.A., Fiege, A., Simon, A.C., Parat, F., Stechern, A., 2017. Co-variability of S6+, S4+, and S2– in apatite as a function of oxidation state: Implications for a new oxybarometer. Am. Min. 102 (3), 548–557.
Konecke, B.A., Fiege, A., Simon, A.C., Linsler, S., Holtz, F., 2019. An experimental calibration of a sulfur-in apatite oxybarometer for mafic systems. Geochim. Cosmochim. Acta 265, 242–258.
Kusebauch, C., John, T., Whitehouse, M.J., Klemme, S., Putnis, A., 2015. Distribution of halogens between fluid and apatite during fluid-mediated replacement processes. Geochim. Cosmochim. Acta 170, 225–246.
La Cruz, N., Simon, A.C., Wolf, A., Reich, M., Barra, F., Gagnon, J., 2019. The geochemistry of apatite from the Los Colorados Kiruna-type iron oxide - apatite deposit, Chile: implications for ore genesis. Mineralium Deposita. https://doi.org/10.1007/s00126-019-00861-z.
La Cruz, N., Ovalle, J.T., Simon, A.C., Konecke, B.A., Barra, F., Leisen, M., Reich, M., Childress, T.M., 2020. The geochemistry of magnetite and apatite from the El Laco Kiruna-type iron oxide–apatite deposit, Chile: Implications for ore genesis. Econ. Geol. 115 (7), 1461–1491.
Le Bas, M.J., Lemaitre, R.W., Streckeisen, A., Zanettin, B., 1986. A chemical classification of volcanic–rocks based on the total alkali silica diagram. Journal of Petrology 27, 745–750.
Mokhtari, M.A.A., Zadeh, G.H., Emami, M.H., 2013. Genesis of iron-apatite ores in Posht-e-Badam block (central Iran) using REE geochemistry. J. Earth Syst. Sci. 2013 (122), 795–807.
Nystrom, J.O., Henríquez, F., 1994. Magmatic features of iron ores of the Kiruna type in Chile and Sweden; ore textures and magnetite geochemistry. Econ. Geol. 89,820–839.
Ovalle, J.T., La Cruz, N.L., Reich, M., Barra, F., Simon, A.C., Konecke, B., Rodriguez-Mustafa, M.A., Childress, T., Deditius, A., Morata, D., 2018. Formation of massive iron deposits linked to explosive volcanic eruptions. Sci. Rep. 8, 14855. https://doi.org/10.1038/s41598-018-33206-3.
Palma, G., Barra, F., Reich, M., Valencia, V., Simon, A.C., Vervoort, J., Leisen, M., Romero., 2019. Geochimica et Cosmochimica Acta 246 515–540.
Pearce, J.A., Peate, D.W., 1995. Tectonic implications of the composition of volcanic arc magmas. Annu. Rev. Earth Planet. Sci. 23 (1), 251–285.
Pearce, J.A., Harris, N.B., Tindle, A.G., 1984. Trace element discrimination diagrams for the tectonic interpretation of granitic rocks. J. Petrol. 25, 956–983.
Peccerillo, A., Taylor, S.R., 1976. Geochemistry of Eocene calcalkaline volcanic rocks from the Kastamonu area, northern Turkey. Contrib. Mineral. Petrol. 58, 63–81.
Piccoli, P.M., Candela, P.A., 2002. Apatite in Igneous Systems. In Phosphates: geochemical, geobiological, and materials importance (Eds. M.J. Kohn, Rakovan, J. M. Hughes). Rev. Mineral. Geochem. 48, 255–292.
Prowatke, S., Klemme, S., 2006. Trace element partitioning between apatite and silicate melts. Geochim. Cosmochim. Acta 70, 4513–4527.
Ramezani, J., Tucker, R.D., 2003. The Saghand region, Central Iran: U-Pb geochronology, petrogenesis and implications for Gondwana tectonics. Am. J. Sci. 303, 622–665.
Sepidbar, F., Moghadam, H.S., Li, C., Stern, R.J., Jiantang, P., Vesali, Y., 2020. Cadomian magmatic rocks from zarand (SE Iran) formed in a Retro-Arc Basin. Lithos 105569.
Sidder, G.B., Day, W.C., Nuelle, L.M., Seeger, C.M., Kisvarsanyi, E.B., 1993. Mineralogic and fluid-inclusion studies of the Pea Ridge depositiron-rare-earth-element deposit. Southeast Missouri. 2039, 205–216.
Sillitoe, R.H., Burrows, D.R., 2002. New field evidence bearing on the origin of the El Laco magnetite deposit, northern Chile. Econ. Geol. 97 (5), 1101–1109.
Simon, A.C., Kniping, J., Reich, M., Barra, F., Deditius, A.P., Bilenker, L., Childress, T., 2018. Kiruna-Type Iron Oxide-Apatite (IOA) and Iron Oxide Copper-Gold (IOCG) Deposits form by a combination of igneous and magmatic-hydrothermal processes: evidence from the Chilean Iron Belt. SEG Special Publications 21, 89–114.
Stormer, J.C., Pierson, M.L., Tacker, R.C., 1993. Variation of F and Cl X-ray intensity due to anisotropic diffusion in apatite during electron microprobe analysis. American Mineralogist 78, 641–648.
Stosch, H., Romer, R., Daliran, F., Rhede, D., 2011. Uranium-lead ages of apatite from iron oxide ores of the Bafq District. East-Central Iran. Miner. Deposita 46, 9–21. https://doi.org/10.1007/s00126-010-0309-4.
Sun, S.-S., McDonough, W.-S., 1989. Chemical and isotopic systematics of oceanic basalts: implications for mantle composition and processes. Geological Society, London, Special Publications 42, 313–345.
Taghipour, S., Kananian, A., Somarin, A.K., 2013. Mineral chemistry and alteration parageneses of the Chogart iron oxide-apatite occurrence, Bafq district, central Iran. Neues Jahrb. Geol. Paläontol. Abh. 2013 (269), 221–240.
Torab, F.M., Lehmann, B., 2007. Magnetite-apatite deposits of the Bafq district, Central Iran: apatite geochemistry and monazite geochronology. Mineral. Mag. 71 (3), 347–363.
Treloar, P.J., Colley, H., 1996. Variations in F and Cl concentrations in apatites from magnetite-apatite ores in northern Chile, and their ore-genetic implications. Mineral. Mag. 60, 285–301.
Velasco, F., Tornos, F., Hanchar, J.M., 2016. Immiscible ironand silica-rich melts and magnetite geochemistry at the El Laco volcano (northern Chile): evidence for a magmatic origin for the magnetite deposits. Ore Geolg. Rev. 79, 346–366.
Westhues, A., Hanchar, J.M., Whitehouse, M.J., Martinsson, O., 2016. New constraints on the timing of host-rock emplacement, hydrothermal alteration, and iron oxide-apatite mineralization in the Kiruna District, Norrbotten, Sweden. Econ. Geol. 111 (7), 1595–1618.
Westhues, A., Hanchar, J.M., LeMessurier, M.J., Whitehouse, M.J., 2017a. Evidence for hydrothermal alteration and source regions for the Kiruna iron oxide – apatite ore (northern Sweden) from zircon Hf and O isotopes. Geology 45 (6), 571–574.
Westhues, A., Hanchar, J.M., Voisey, C.R., Whitehouse, M.J., Rossman, G.R., Wirth, R., 2017b. Tracing the fluid evolution of the Kiruna iron oxide apatite deposits using zircon, monazite, and whole rock trace elements and isotopic studies. Chem. Geol. 466, 303–322.
Zeng, L.-P., Zhao, X.-F., Li, X.-C., Hu, H., McFarlane, C., 2016. In situ elemental and isotopic analysis of fluorapatite from the Taocun magnetite-apatite deposit, Eastern China: constraints on fluid metasomatism. Am. Min. 101 (11), 2468–2483.
Zhao, X.-F., Zhou, M.-F., Gao, J.-F., Li, X.-C., Li, J.-W., 2015. In situ Sr isotope analysis of apatite by La-MC-ICPMS: constraints on the evolution of ore fluids of the Yinachang Fe-Cu-REE deposit, Southwest China. Miner. Deposita 50 (7), 871–884.
Zhu, C., Sverjensky, D.A., 1991. Partitioning of F-Cl-OH between minerals and hydrothermal fluids. Geochim. Cosmochim. Acta 55, 1837–1858.
Ziapour, S., Esmaili, D., Khoshnoodi, K., Niroomand, S., Simon, A.C., 2021, Mineralogy, geochemistry, and genesis of the Chahgaz (XIVA Anomaly) Kiruna-type iron oxide-apatite (IOA) deposit, Bafq district, Central Iran. Ore Geol. Rev. 128.